Chemical Engineering Science 334 (2026) 124245

Contents lists available at ScienceDirect

Chemical Engineering Science

journal homepage: www.elsevier.com/locate/ces

A particle-resolved CFD analysis of kinetic modeling based on profile reactor data using pseudo-continuum models

Gerrit Küchen [a,*], Martin Kutscherauer [b], Stefan Rudolph [b], Gregor D. Wehinger [b], Thomas Turek [a]

[a] Institute of Chemical and Electrochemical Process Engineering, Clausthal University of Technology, Leibnizstr. 17, Clausthal-Zellerfeld, 38678, Germany
[b] Institute of Chemical Process Engineering, Karlsruhe Institute of Technology, Kaiserstr. 12, Karlsruhe, 76131, Germany

ARTICLE INFO

Keywords:
Profile reactor
Particle-resolved reactive CFD
Pseudo-continuum models
Reaction kinetic modeling
CO_2 methanation

ABSTRACT

Profile reactors enable the acquisition of spatially resolved concentration and temperature profiles in fixed bed reactors and have developed into an important laboratory tool in heterogeneous catalysis. However, the quantitative evaluation of such data for kinetic modeling is often accompanied by input and reactor model uncertainties, particularly with respect to heat and mass transfer as well as the impact of the sampling capillary. In this work, we combine experimentally validated particle-resolved reactive CFD of a profile reactor for the CO_2 methanation reaction on a Ni/Al_2O_3 catalyst with a systematic assessment of heterogeneous and homogeneous pseudo-continuum models. Homogeneous pseudo-continuum models proved incapable of adequately describing product selectivity, while heterogeneous models, even when considering the influence of the sampling capillary and adjusted boundary conditions at the reactor walls, still cannot describe heat transport within the reactor correctly, leading to erroneous kinetic parameters. Neglecting the evaluation of the energy balance and inserting the measured average temperature profile directly into computationally efficient one-dimensional models can yield improved results by circumventing these model uncertainties. However, this procedure is only viable when the reaction rate can be linearized with sufficient accuracy over the radial temperature range. To verify this prerequisite, we derive a condition that can be easily evaluated numerically a posteriori, based on measured quantities in the profile reactor and the obtained reaction kinetics, ultimately enhancing the efficient utilization of profile reactors in kinetic research.

1. Introduction

Profile reactors have recently gained increased attention in heterogeneous catalysis research, as they enable the efficient generation of comprehensive datasets for studying reaction kinetics, resolving reaction networks, and investigating reactor dynamics (Korup et al., 2011). In general, these tubular or plate reactors contain a fixed bed or a layer of porous, catalytically active material to facilitate chemical reactions. Also, such reactors provide invasive or non-invasive probing mechanisms for obtaining spatially resolved profiles of relevant quantities such as gas-phase composition and temperature, the oxidation state of the catalyst, and surface species present during operation (Horn et al., 2010; Hernandez Lalinde et al., 2020; Cholewa et al., 2024; Shirsath et al., 2023; Wolke et al., 2021). Early work to develop profile reactors for various applications was conducted by Horn et al. (2006, 2007, 2010), who embedded a capillary comprising orifices for defined sampling of the gas phase inside fixed beds, on the example of the partial catalytic oxidation of ethane. A repeatable relative displacement of the fixed bed with respect to the capillary allows for the systematic measurement of temperature and concentration profiles. Later, a comparable setup was used to investigate the Fischer–Tropsch synthesis on iron-based catalysts (Wolke et al., 2021). Cholewa et al. (2024) investigated the ammonia synthesis on ruthenium- and iron-based catalysts using a larger-scale profile reactor ($d_R = 8$ mm) to derive kinetic parameters from the measured temperature and conversion profiles. For the selective oxidation of ethylene, a thorough investigation of reaction kinetics and inhibition mechanisms based on both reactor profiles and experiments in differential reactors was conducted by Berg et al. (2024). In the context of CO and CO_2 methanation, pioneering research was carried out by Kopyscinski et al. (2010) and Hernandez Lalinde et al. (2018, 2020), who performed axially resolved measurements in a coated plate reactor using Ni/Al_2O_3 catalysts. Coupled with DRIFTS measurements to identify ad-

* Corresponding author.
E-mail address: kuechen@icvt.tu-clausthal.de (G. Küchen).

https://doi.org/10.1016/j.ces.2026.124245
Received 13 March 2026; Received in revised form 30 April 2026; Accepted 13 May 2026
Available online 16 May 2026

Nomenclature

Latin symbols

a_{Ni}	Nickel surface area [$m^2\ g^{-1}$]
A_h	Hydraulic cross-sectional area [m^2]
c	Concentration [$mol\ m^{-3}$]
d	Diameter [m]
$\mathbf{D}$	Deformation tensor
D	Dispersion [%]
$D_{i,k}$	Binary diffusion coefficient [$m^2\ s^{-1}$]
$D_{mix,i}$	Diffusion coefficient in the mixture [$m^2\ s^{-1}$]
$D_{rad,ax,i}$	Dispersion coefficient [$m^2\ s^{-1}$]
E	Error [%]
E_A	Activation energy [$kJ\ mol^{-1}$]
f_k	Factor [-]
h_i	Mass specific enthalpy [$kJ\ kg^{-1}$]
h_{wall}	Wall thickness [m]
$\mathbf{I}$	Identity tensor
K_i	Adsoption constant [$bar^{0.5}$] or [bar]
K_j	Equilibrium constant [–] or [bar^2]
k_i	Rate constant [$mol\ kg^{-1}\ s^{-1}$]
L	Length [m]
$\tilde{M}$	Molar mass [$kg\ mol^{-1}$]
$\dot{n}_i$	Molar flow rate [$mol\ s^{-1}$]
N	Number [-]
p	Pressure [Pa] or [bar]
p_i	Partial pressure [Pa] or [bar]
Q_{H_2}	Hydrogen adsorption capacity [$\mu mol\ g^{-1}$]
r, r_c, r_{cap}, z	Dimensionless coordinates [-]
$\dot{r}_j$	Reaction rate [$mol\ kg^{-1}\ s^{-1}$]
R	Radius [m]
$\Re$	Ideal gas constant [$J\ mol^{-1}\ K^{-1}$]
S_{CH_4}	Methane selectivity [–]
SSA	Specific surface area [$m^2\ g^{-1}$]
$\mathbf{T}$	Viscous stress tensor
T	Temperature [K]
$\bar{T}$	Average temperature [K]
$\mathbf{u}$	Gas velocity vector [$m\ s^{-1}$]
U	Heat transfer coefficient [$W\ m^{-2}\ s^{-1}$]
u_r	Radial gas velocity [$m\ s^{-1}$]
u_t	Tangential gas velocity [$m\ s^{-1}$]
u_{ax}	Axial gas velocity [$m\ s^{-1}$]
$u_{s,ax}$	Superficial axial velocity [$m\ s^{-1}$]
V_{pore}	Pore volume [$cm^3\ g^{-1}$]
$\dot{V}$	Volume flow rate [$m^3\ s^{-1}$]
w_i	Weight fraction [–]
X_{CO_2}	Conversion [–]
y_i	Molar fraction [–]
$\tilde{r}, \tilde{r}_c, \tilde{r}_{cap}, \tilde{z}$	Coordinates [m]
ΔH_i	Adsorption enthalpy [$kJ\ mol^{-1}$]
$\Delta H^0_{R,j}$	Reaction enthalpy [$kJ\ mol^{-1}$]

Greek symbols

2Θ	Bragg angle [°]
α_{wall}	Wall heat transfer coefficient [$W\ m^{-2}\ K^{-1}$]
α^{fc}	Heat transfer coefficient [$W\ m^{-2}\ K^{-1}$]
β_i^{fc}	Mass transfer coefficient [$m\ s^{-1}$]
γ	Discretization error [-]
η_j	Catalyst effectiveness factor [–]
ε_{bed}	Bed porosity [–]
λ	Wavelength [Å]
$\lambda_{ax,\ rad}$	Effective thermal conductivity [$W\ m^{-1}\ K^{-1}$]
∇	Nabla operator
$\nu_{i,j}$	Stoichiometric coefficient of species i in reaction j [–]
π	Pi [–]
ρ	Density [$kg\ m^{-3}$]
τ	Tortuosity [–]

Abbreviations

1D	One-dimensional
2D	Two-dimensional
COmeth	CO methanation
CPR	Compact Profile Reactor
Di	Dirichlet
DRIFTS	Diffuse reflectance infrared Fourier transform spectroscopy
FID	Flame ionization detector
GC	Gas Chromatograph
LHHW	Langmuir-Hinshelwood-Hougen-Watson
PRCFD	Particle resolved computational fluid dynamics
PtG	Power-to-Gas
Ro	Robin
rWGS	reverse Water-Gas-Shift
TCD	Thermal conductivity detector

Subscripts and superscripts

C	Component
c	Catalyst
cap	Capillary
cf	Averaged catalyst-fluid phase
eff	Effective
eq	Equilibrium
f	Fluid
f	fine
fb	Fixed bed
g	Gas
i	Component
i	inside
in	Inlet
m	medium
max	Maximum
o	outside
out	Outlet
p	Particle
pore	Pore
R	Reactor
R	Reaction
ref	Reference
rel	Relative
surf	Surface

sorbed surface intermediates and a one-dimensional reactor model, the authors identified the most likely reaction pathways and parameterized the resulting kinetic rate equations considering the reverse water–gas-shift (rWGS) and direct CO_2 methanation reactions.

In another work, the reaction kinetics for a Ni/SiO_2 catalyst produced via spray pyrolysis were derived based on spatially resolved profiles (Küchen et al., 2026). Shirsath et al. (2023) recorded spatially resolved temperature and concentration profiles over gamma alumina based nickel and nickel iron catalysts and compared the obtained profiles with numerical results implementing microkinetic considerations (Schmider et al., 2021).

Once the obtained spatial profiles are to be evaluated quantitatively for kinetic modeling, numerical models of the employed profile reactors become necessary. These models should represent the relevant transport phenomena as accurately as possible to enable reliable conclusions. Typically, pseudo-continuum models are chosen, which offer an attractive trade-off between accuracy, numerical stability, and computational cost. However, in the current literature, the energy balance in these models is often not evaluated and the measured axial temperature profile is inserted directly in the model. This simplification is usually justified by assuming negligible radial temperature gradients or isothermal conditions (Hernandez Lalinde et al., 2020). Using the measured temperatures in the reactor model reduces the required computational cost and eliminates significant uncertainties in the mathematical description of heat transport in the reactor (Shirsath et al., 2023; Cholewa et al., 2024). If the energy balance is evaluated, significant discrepancies between modeled and experimental values have been reported (Berg et al., 2024). To further improve the utilization of profile reactors in reaction engineering research, profound knowledge of the conditions inside such reactors is of paramount importance. Detailed multiscale heterogeneous modeling techniques, such as particle-resolved reactive CFD (PRCFD) simulations, can contribute to improving the understanding of the conditions present in laboratory-scale profile reactors (Wehinger et al., 2022). Such computationally highly demanding approaches enable the combined first-principles modeling across different scales, from reactions at the catalyst surface and diffusive transport inside porous catalyst particles up to the macroscopic reactor behavior. Significant progress in the integration of reaction kinetics into CFD simulations has been summarized in reviews by Dixon and Partopour (2020) and Jurtz et al. (2019). Since PRCFD simulations allow resolving inter- and intraparticle transport coupled with catalytic reactions, recent applications have predominantly focused on highly exothermic and endothermic processes carried out in slender fixed bed reactors (Kutscherauer and Wehinger, 2025; Partopour and Dixon, 2018; Dixon, 2021; Maffei et al., 2016; Kutscherauer et al., 2024). For example, Kutscherauer and Wehinger (2025) performed PRCFD simulations for the partial methanol and butane (Kutscherauer et al., 2024) oxidation and quantified the impact of the chosen reaction and boundary conditions on local phenomena inside the fixed bed, which ultimately affect the overall conversion and selectivity. Wehinger et al. (2016) conducted PRCFD simulations of the methane dry reforming process on nickel and found good agreement with spatially resolved experimental data, highlighting the complex interactions of local transport phenomena and kinetics, which can be resolved in PRCFD simulations without depending on empirical transport correlations. Overall, insights gained from PRCFD simulations of profile reactors can substantially enhance the understanding of the local conditions prevailing in such systems and support the refinement and validation of the assumptions commonly employed in pseudo-continuum reactor models.

The CO_2 methanation reaction, a crucial part of Power-to-Gas (PtG) technologies, is investigated in this study. Next to the direct hydrogenation of carbon dioxide to methane according to Eq. 1, the reaction path via the rWGS reaction (Eq. 2) with the consecutive methanation of carbon monoxide (COmeth, Eq. 3) is present as well. The direct carbon dioxide methanation reaction is strongly exothermic and can lead to the formation of distinct temperature hot spots in the typically employed tubular reactors. The occurrence of the intermediate product carbon monoxide is usually most pronounced around the temperature hot spot, given the rWGS is an endothermic reaction. Typical industrial methanation conditions include temperatures of 473 to 673 K, absolute pressures of 1 to 20 bar, and a H_2/CO_2 ratio close to 4 (Lee et al., 2021; Rönsch et al., 2016). The kinetics of these reactions are commonly formulated using Langmuir–Hinshelwood–Hougen–Watson (LHHW) type models assuming different combinations of the described reaction network (Eq. 1 to 3) (Langer et al., 2023; Xu and Froment, 1989; Koschany et al., 2016; Burger et al., 2021). In this work, the reaction kinetics recently published by Langer et al. (2023), comprising a sequence of rWGS and carbon monoxide methanation reactions, are employed for a 10 wt% Ni/Al_2O_3 catalyst synthesized by incipient wetness impregnation.

$$CO_2 + 4\,H_2 \rightleftharpoons CH_4 + 2\,H_2O \quad (1)$$

$$CO_2 + H_2 \rightleftharpoons CO + H_2O \quad (2)$$

$$CO + 3\,H_2 \rightleftharpoons CH_4 + H_2O \quad (3)$$

In this work, we combine experimentally validated PRCFD simulations of a profile reactor for the CO_2 methanation reaction with a systematic assessment of heterogeneous and homogeneous pseudo-continuum models to (i) elaborate how input and physical reactor model uncertainties can bias the fitted kinetic parameters and (ii) derive conditions under which the energy balance can be neglected in the model-based evaluation and the parameter fit can be based solely on measured radially averaged quantities, ultimately yielding more precise results. For the latter, we propose a condition involving the wall temperature T_{wall}, the measured hot spot temperature $\bar{T}_{f,max}$, and the fitted reaction kinetics that can be easily tested a posteriori. Overall, this investigation contributes to an improved implementation and understanding of profile reactors in catalysis research.

2. Materials and Methods

2.1. Experimental

2.1.1. Catalyst synthesis and pretreatment

A 10 wt% Ni/Al_2O_3 catalyst was prepared by incipient wetness impregnation. Nickel(II) nitrate hexahydrate (Puratronic grade, Merck) was dissolved in ultrapure water produced by a Sartorius Arium system (0.055 µS cm^{-1}). The resulting solution was impregnated onto the alumina support (Puralox Granules 400/200, Sasol), composed of spherical particles with an average diameter of $d_{p,50} = 412$ µm. The mass ratio of nickel(II) nitrate hexahydrate to the support material was adjusted to yield the desired nickel loading. The narrow particle size distribution is displayed in the supporting information (Section S1). After impregnation, the material was dried at 363 K for 6 h and then calcined in air at 723 K for 6 h using a muffle furnace. Prior to catalytic experiments, the catalyst was activated by reduction at 673 K for 3 h with a mixture of 10 mol% hydrogen in argon. The long-term stability of the Ni/Al_2O_3 catalyst was verified through a steady-state experiment conducted over 50 h at 653 K (SI Section S2).

2.1.2. Physical and Chemical Charazerization

The specific surface area (SSA) of the particles was determined by BET analysis (3Flex, Micromeritics Instruments Corp.) using nitrogen adsorption. X-ray diffraction (XRD) was employed for crystallographic characterization of the catalyst powders (Empyrean, Malvern Panalytical Ltd., Bragg–Brentano configuration, Cu Kα, $\lambda = 1.5406$ Å, scan rate 8 ° min^{-1}). The density and pore diameter were measured using a helium pycnometer (Pycnomatic ATC, Porotec) and a mercury porosimeter (Pascal 140/440 Series, Thermo Scientific), respectively. Nickel dispersion D, nickel surface area a_{Ni}, and crystallite size $d_{crystallite}$ were derived from hydrogen pulse experiments. The detailed experimental procedure is described in our previous works (Küchen et al., 2024; Küchen and Turek, 2026), based on the method developed by Friedland et al. (2020). All relevant chemical and physical properties are summarized in Table 1. These are consistently in the typical range for supported alumina catalysts produced by incipient wetness impregnation.

2.1.3. Profile reactor

Methanation experiments were performed in a Compact Profile Reactor (CPR, REACNOSTICS GmbH), which enables spatially resolved measurements of gas composition and temperature along an integral fixed bed reactor. A silica-coated capillary positioned at the center of the tubular quartz reactor and equipped with four radially arranged orifices allows defined extraction of gas samples. These sampling flow rates are

Table 1
Summary of physical properties of the 10 wt% Ni/Al_2O_3 catalyst. Catalyst specific surface area SSA, pore volume V_{pore}, hydrogen adsorption capacity Q_{H_2}, Ni surface area a_{Ni}, Ni crystallite diameter $d_{crystallite}$, dispersion D, apparent density ρ_c, thermal conductivity λ_c, tortuosity τ_c, and pore diameter d_{pore}. The XRD diffractogram is depicted in the supporting information (Section S3).

Property	Value	Unit	Method
a_{Ni}	8.3	$m^2\ g^{-1}$	H_2 chemisorption
D	12.3	%	H_2 chemisorption
$d_{crystallite}$	8.1	nm	H_2 chemisorption
d_{pore}	9.3	nm	Hg porosimetry
λ_c	0.15	$W\ m^{-1}\ K^{-1}$	assumed based on Langer and Freund (2024)
ρ_c	1.704	$g\ cm^{-3}$	Hg porosimetry and He pycnometry
Q_{H_2}	104.6	$\mu mol\ g^{-1}$	H_2 chemisorption
SSA	188	$m^2\ g^{-1}$	N_2 sorption
τ_c	3	-	assumed based on Donaubauer and Hinrichsen (2019), Fischer et al. (2019)
V_{pore}	0.39	$cm^3\ g^{-1}$	N_2 sorption

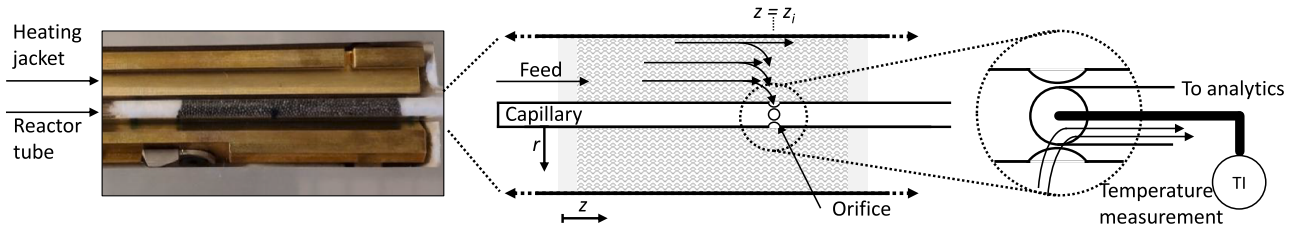

Fig. 1. Details of the reactor and sampling mechanism.

typically kept below 5 % of the total flow rate to minimize disruptions of the flow field in the reactor (Wollak et al., 2022). The extracted gas is directed to a gas chromatograph (Trace 1300, Thermo Fisher Scientific), equipped with an FID and two TCDs and calibrated for the components H_2, CO_2, CH_4, CO, and N_2, with nitrogen used as an internal standard, while the local temperature is measured by a thermocouple whose tip is located adjacent to the orifices. Axial profiles of temperature and gas composition are obtained by moving the reactor relative to the fixed capillary. Temperature control of the reactor is achieved using a heating block that is tightly interlocked around the reactor tube. The actual temperature at the thermocouple tip is proposed to result from an interplay between conduction through the stainless-steel capillary, radiation and convective heat transfer while the measured temperature is assumed to be biased towards the actual gas-phase temperature (Horn et al., 2006; Korup et al., 2011). Accordingly, the measured temperature is treated as the radially averaged gas-phase temperature throughout this manuscript, as illustrated in Figure 1, along with additional details of the reactor setup. Consequently, the composition of the extracted sample gas is likewise assumed to represent a radial average.

Throughout this investigation, three experimental cases were considered at constant pressure and flow rate, with varying inlet temperatures (593, 613, and 633 K). The accuracy and consistency of the gas analysis were assessed using the carbon balance (SI Section S4), which was consistently closed within ±2 % for all experiments. The void fraction reached in the experiments $\epsilon_{bed,experiment}$ was determined based on the total volume and mass of the packed bed, the mass per catalyst particle, and the mean particle diameter. Details on the reactor and capillary geometry, the catalyst fixed bed and the investigated reaction conditions are summarized in Table 2 and in Figure 2.

Table 2
Summary of reactor, catalyst, and fixed bed geometry, as well as the reaction conditions of the three investigated cases: mean particle diameter $d_{p,50}$, thickness of the reactor wall h_{wall}, length of the fixed bed L_{fb}, inner (i) and outer (o) radii R of the reactor (R), and capillary (cap), and the bed porosity ϵ_{bed}. The reactor radii correspond to the dimensions of the annular gap that results from inserting the capillary into the reactor tube. Pressures are given as absolute pressures. Standard conditions: $T_{std} = 273.15$ K, $p_{std} = 1$ atm.

Property	Value	Unit
$d_{p,50}$	412	µm
h_{wall}	1.5	mm
$L_{fb,experiment}$	30.0	mm
$L_{fb,PRCFD}$	14.9	mm
$R_{cap,o}$	0.4	mm
$R_{cap,i}$	0.25	mm
$R_{R,i}$	0.4	mm
$R_{R,o}$	1.5	mm
$\epsilon_{bed,experiment}$	0.38	-
$\epsilon_{bed,PRCFD}$	0.41	-
p_{out}	2	bar
T_{in}	593, 613, 633	K
$\dot{V}_{in}$	14.04	L_N/h
$y_{CO_2,in}$	0.05	-
$y_{H_2,in}$	0.20	-
$y_{N_2,in}$	0.75	-

2.2. Numerical methods

2.2.1. Particle resolved computational fluid dynamics

The applied particle resolved computational fluid dynamics (PRCFD) approach can be divided into three main steps: (i) generating the fixed bed geometry, (ii) discretizing the geometry with a finite volume mesh and (iii) solving the governing equations based on this mesh (Jurtz et al., 2019; Kutscherauer, 2024). A detailed description of the governing equations for modeling the fluid and catalyst domain, as well as the capillary can be found in the supporting information (Section S5).

Fixed bed and mesh generation

The fixed bed geometry is generated synthetically with the rigid body approach implemented in the open source game engine Blender 2.79 using a filling algorithm developed by Partopour and Dixon (2017) and extended by Kutscherauer (2024). The capillary centered in the reactor tube is already considered in the filling procedure to describe its disturb-

ing effect on the structure of the packed bed (Kutscherauer et al., 2023). The spherical catalyst particles are dropped separately at randomized positions within a defined region 20 mm above the bottom of the reactor tube. This region is defined using cylindrical coordinates so that, when inserted, the particles do not touch the reactor or the capillary wall. After insertion, the spheres fall down due to gravity and fill the reactor tube. The diameter distribution of the catalyst spheres used in the experiment can be described using a Gaussian with a mean diameter $d_{p,50}$ of 412 µm (SI Section S1). To accurately capture the fixed bed morphology, the size of the inserted particles follows these experimentally determined distribution. The resulting fixed bed contains 1500 particles, corresponding to a height of 14.9 mm, and the integral void fraction $\varepsilon_{bed,PRCFD}$. The deviation between the void fraction of the experimental and the synthetically generated fixed bed can mainly be attributed to the high measurement error in the catalyst particle mass (10 %). Taking this into account, the agreement between the simulated and experimental void fractions can be considered sufficiently accurate.

The Siemens Simcenter STAR-CCM+ meshing algorithm is applied to generate the calculation mesh with polyhedral cells based on the as STL file exported fixed bed geometry. To keep the computational effort within reasonable limits, the wall thickness, the hole, and the interior of the capillary are not resolved. During the mesh generation procedure, the particle-particle and particle-wall contacts are modified using the local caps method (Eppinger et al., 2011). Contact modification is mandatory in fixed bed mesh generation, as it allows zero-dimensional point contacts to be resolved without erroneous meshes or unfeasible mesh refinement close to the contact regions (Dixon et al., 2013-01; Pichler et al., 2021-01; Kutscherauer et al., 2022). In the local caps method, the contact point is replaced with a gap that is filled with fluid cells. This gap is smaller than 0.8 % of $d_{p,50}$, resulting in a high-quality mesh and ensuring a solution that is independent of the contact modification (Kutscherauer et al., 2022). The base size, which characterizes the cell size in Siemens Simcenter STAR-CCM+ is set to the mean particle diameter and the size of the surface cells is specified as 5 % of the base size. Three layers of prismatic cells with a total thickness of 5 % of the base size are generated at the inner and outer particle surface as well as at the tube and capillary wall to efficiently resolve boundary layers. To improve mesh quality in the contact regions, the number of prismatic cells is reduced or completely rejected and the surface mesh is refined for close proximity surfaces. A mesh dependency study is conducted, showing that the applied mesh resolution provides a physically accurate solution while keeping the computational effort feasible. The final mesh consists of 22.6 million cells for the fluid region and 23.1 million cells for the catalyst domain. The details of the mesh dependency study are given in the supporting information (Section S5).

Simulation setup

The PRCFD simulations delineate the initial 14.9 mm from the inlet downstream of the catalytic fixed bed within the profile reactor. To avoid influencing the results through outlet effects, only the first 13 mm of the fixed bed is used for comparison with the experimental measurements and further evaluations. Figure 2a shows a section of the generated mesh, while Figure 2b illustrates the simulation setup and applied boundary conditions. At the inlet, the temperature, gas composition, and velocity are specified. The inlet velocity is calculated from the flowrate $\dot{V}_{in}$. Additionally, the outlet pressure and wall temperature are set. The values of these inlet, outlet, and tube wall boundary conditions are taken from the experimental operating conditions. For the velocity, a no-slip boundary condition is applied to the catalyst surface, the tube, and the capillary wall. To prevent unphysical backflow at the outlet boundary, an empty tube section is added between the end of the fixed bed and the outlet.

Mesh generation and all simulations are carried out with the commercial software Siemens Simcenter STAR-CCM+ 2310.10. The governing equations are solved based on the computation mesh using the SIMPLE algorithm. The detailed numerical methodology is described elsewhere (Kutscherauer et al., 2024). Convergence is monitored at each iteration step by evaluating the residuals and several engineering quantities, such as pressure drop and conversion, as well as the closure of the overall mass, energy, and species mass conservation. All simulations are performed on 640 CPUs of the high-performance computing server bwUniCluster 3.0 with Intel Xenon Platinum 8358 processors at 2.6 GHz and 200 GB RAM. After approximately 80 000 iterations, one simulation converges, which takes about six days.

Table 3
Overview of the basic pseudo-continuum model configurations used throughout this manuscript.

Model name	Dimensions	Catalyst Efficiency	Boundary Condition	Capillary
Hom1D$^{\eta}$	1D	✓	-	-
Het1D	1D	-	-	-
Het1D$_{\alpha_{wall}\to\infty}$	1D	-	-	-
Het2D$_{Ro}$	2D	-	Ro	-
Het2D$_{Ro,cap}$	2D	-	Ro	✓
Het2D$_{Di,cap}$	2D	-	Di	✓

2.2.2. Continuum models

Pseudo-continuum models, which require a substantially lower amount of computational effort than PRCFD simulations, with different levels of detail are used throughout this work for comparison with data obtained from the PRCFD simulations (Fischer et al., 2019; Kreitz et al., 2019). We investigated six different pseudo-continuum models, which are formulated either homogeneously (Hom) or heterogeneously (Het), and which differ in dimensionality (1D or 2D), in the boundary condition applied at the reactor walls, namely Robin (Ro) or Dirichlet (Di) conditions, and in the inclusion of the capillary (cap). In homogeneous pseudo-continuum models, the catalyst effectiveness factor η is derived from the Thiele modulus, assuming the rWGS reaction as the rate-limiting reaction and carbon dioxide as the diffusion-limiting species (Elnashaie and Abashar, 1993). A Robin boundary condition accounts for a finite wall heat transfer coefficient, causing a temperature step between the reactor wall and the fluid phase. When the heat transfer resistance is negligible, this step at the wall disappears, as accounted for by a Dirichlet boundary condition. The nomenclature is summarized in Table 3. The one-dimensional model Het1D$_{\alpha_{wall}\to\infty}$ is based on the same governing equations as the Het1D model. However, when computing the overall heat transfer coefficient U, the heat transfer resistance between the fixed bed and the tube wall is neglected. A schematic of the reactor geometry, including all relevant dimensions, is shown in Figure 2c.

The employed balance equations, boundary conditions, reaction kinetics, and physical properties calculation methods are outlined in the supporting information (Sections S6-8). The kinetic rate equations and parameters are taken from Langer et al. (2023) without additional adaption. The models were implemented in Siemens gPROMS Process® (Version 2023.2.1, Siemens Digital Industries Software (2023)). The axial domain z of the partial differential equation system was discretized using the finite element method into 50 elements, the radial domain r into 10 elements, the particle domain r_c into 15 elements, and the radial capillary domain r_{cap} into 5 elements. The resulting system of differential–algebraic equations was solved with the built-in DAEBDF solver, which applies a variable-step and variable-order backward differentiation scheme.

3. Results and Discussion

Deriving intrinsic reaction kinetics from spatially resolved profiles requires the ability to clearly distinguish between transport and reaction phenomena. The main aim of the following elaboration is to identify a pseudo-continuum model that fits the considered profile reactor best and is suitable for kinetic fitting. Firstly, results from PRCFD simulations

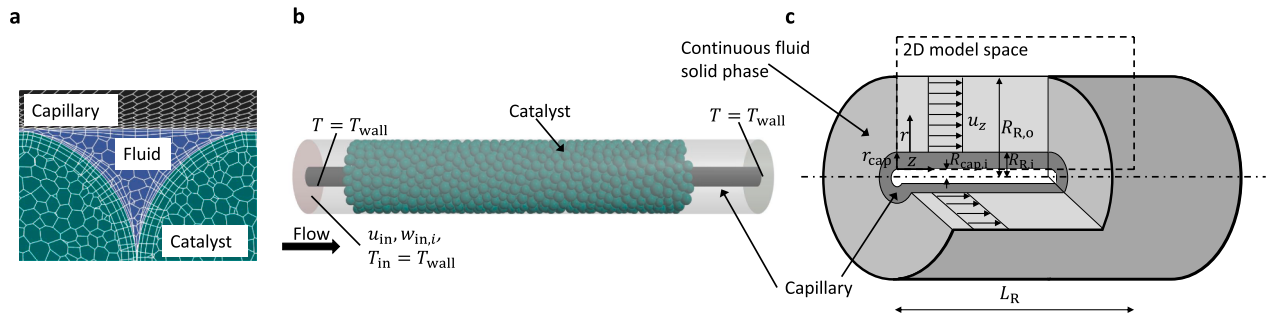

Fig. 2. **a** Mesh including catalyst- and fluid phase as well as the capillary, **b** scheme of the PRCFD simulation setup and **c**, the two-dimensional continuum models.

are validated against experimental data. Secondly, these results are used to evaluate pseudo-continuum models with different levels of detail and boundary conditions to identify the best-fitting model. Then, the impact of the selected model on the fitted kinetic parameters is quantified. To avoid effects of an inaccurate modeling of the heat transport within the reactor on the estimated kinetic parameters, the energy balance has frequently been neglected in the evaluation, and the measured temperature is directly introduced into the model. In the context of kinetic parameter estimation from spatial reaction profiles, this is an appealing simplification, because inaccuracies in the heat transport description do not directly affect the estimated kinetic parameters, while simple one-dimensional models ensure low computational cost. Accordingly, based on the results from the PRCFD simulation, a criterion is derived that specifies under which conditions this latter approach is viable and sufficiently accurate for kinetic modeling.

3.1. Validation of PRCFD simulation with experimental data

The circumferentially and radially averaged spatial molar fraction profiles (Figure 3a–c) and fluid-phase temperature profiles (Figure 3d–f) obtained from the PRCFD simulations are compared with the experimental data over a bed length of 13 mm for all cases investigated. Averaging is performed by computing an area-weighted average over defined cross-sections. The respective standard deviations of the averages are also calculated area-weighted and shown as shaded areas. The respective standard deviations are shown as shaded areas. Regarding the concentration profiles, the experimental and numerical results show overall good agreement in terms of both temperature-dependent trends and quantitative values. Across all inlet temperatures, the overall conversion is slightly overestimated by the PRCFD simulations. However, this discrepancy decreases at higher inlet temperatures. The concentration profiles of the intermediate product carbon monoxide, which exhibit higher peak concentrations at elevated temperatures, are also well captured by the PRCFD simulations. The maximum absolute error in the predicted carbon monoxide concentration is approximately 500 ppm. Because the overall concentration of CO is rather small, these errors can correspond to large relative errors. Since the sign of the relative deviation is temperature dependent, kinetic parameters such as the activation energy and adsorption enthalpies, which were directly adopted from the literature without further modification, are a reasonable cause for this deviation. Considering the rWGS reaction as an endothermic step within an overall highly exothermic process, the slightly differing selectivities would mainly affect the temperature profile. However, this influence is negligible due to the overall low amount of CO formed. Obtained standard deviations from the PRCFD are narrow, indicating a radially homogeneous gas-phase composition in the reactor. The evaluation of the flow fields obtained from the PRCFD simulations indicates that this can mainly be attributed to convective species transport in the lateral direction. Furthermore, no distinct channeling around the capillary can be observed. Such a bypass flow could lead to inaccurate temperature and gas composition measurements. More details on the fixed bed morphology and velocity field can be found in the supporting information (Section S9).

For direct comparison with data obtained from the profile reactor, the gas-phase temperature T_f is extracted from the PRCFD simulations together with the corresponding radial minimum and maximum temperatures (Figure 3d–f). The overall shape of the temperature profiles shows good agreement between simulation and experiment. However, the experimental values are consistently 1 to 2 K lower than those predicted by the PRCFD simulations. Radial temperature gradients resolved in the PRCFD simulations reveal a temperature range in the radial direction of up to 10 K at T_{in} = 593 K, 15 K at T_{in} = 613 K, and 18 K at T_{in} = 633 K, with the largest gradients occurring in the vicinity of the temperature hot spot. The good agreement between the radially averaged temperatures obtained from the PRCFD simulations and the experimental measurements supports the assumptions made regarding the sampling arrangement in the profile reactor, which is presumed to provide a radial average of both temperature and composition. Overall, the PRCFD simulations are sufficiently validated against the experimental data from the profile reactor and are therefore assumed to closely represent the conditions inside the reactor.

3.2. Interparticle heat and mass transport phenomena - Comparison of axial profiles of averaged quantities from PRCFD and pseudo-continuum models

Pseudo-continuum models, especially homogeneous ones, are frequently used to evaluate data from spatially resolved measurements for various purposes, such as kinetic parameter estimation, investigation of reaction networks and pathways, and analysis of dynamic reactor behavior (Cholewa et al., 2024; Hernandez Lalinde et al., 2020; Berg et al., 2024; Wolke et al., 2021). To derive the most accurate conclusions from experiments efficiently, the applied models should resemble the physical reactor as closely as possible while limiting the required computational effort. In the following, profiles of temperature, carbon dioxide conversion, and selectivity to methane obtained from the detailed PRCFD simulations (Figure 4) are compared with results from continuum models of different levels of detail, as described in Section 2.2.2. For the PRCFD simulations, circumferentially and radially averaged profiles are depicted, while radially averaged quantities are considered for the two-dimensional pseudo-continuum models. Since homogenous pseudo-continuum models assume the fluid and catalyst phases to be lumped together, the temperature T_{cf} extracted from the PRCFD simulations and the heterogeneous pseudo-continuum models represents an average of the fluid- and catalyst-phase temperatures.

In general, all considered continuum models predict an increasing carbon dioxide conversion along the entire reactor, accompanied by the formation of a temperature hot spot in the region between $z = 0.4$ and $z = 0.6$. The most significant systematic discrepancies between the PRCFD and the pseudo-continuum models arise in the selectivity, which initially exhibits already high values in the PRCFD due to the employed

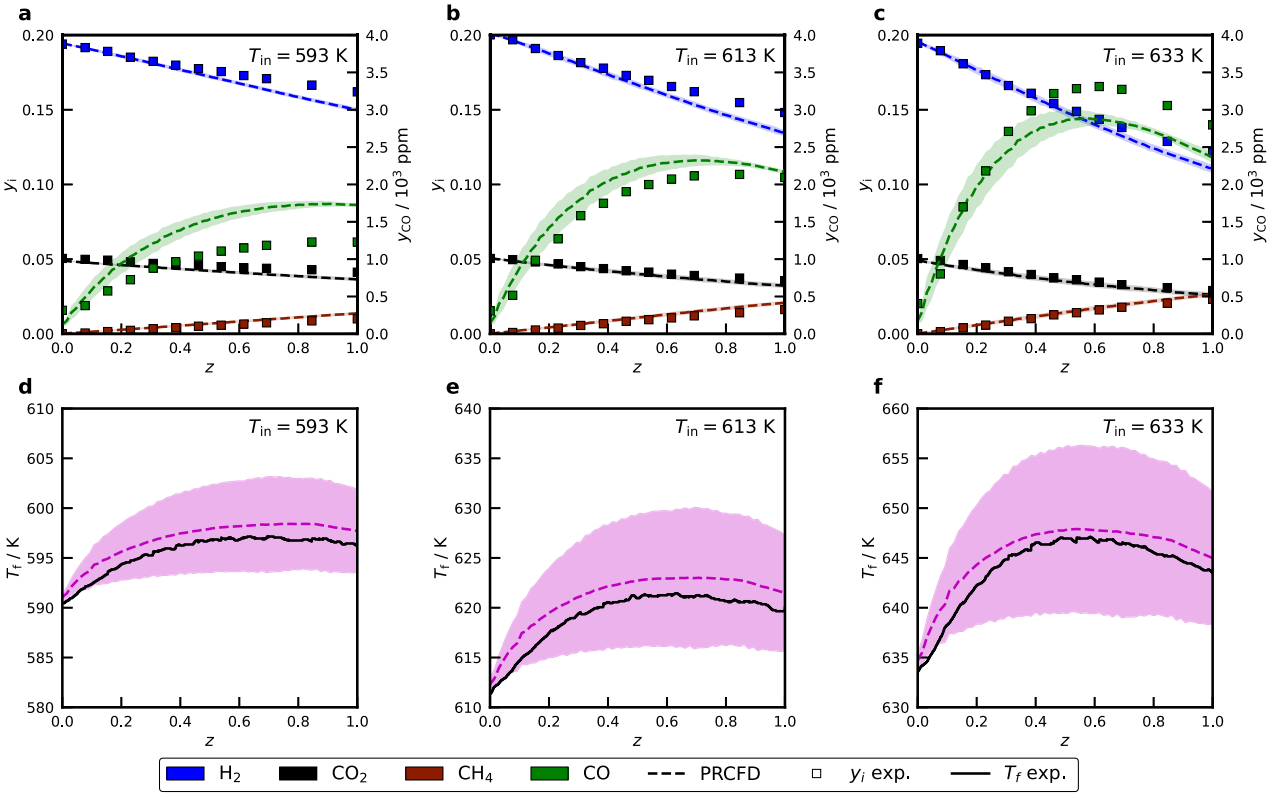

Fig. 3. Comparison of experimental data with results obtained from the PRCFD simulations. The shaded areas represent the respective lateral standard deviations derived from the PRCFD. **a**, **d** show the concentration and temperature profiles for an inlet temperature of T_{in} = 593 K, **b**, **e** for T_{in} = 613 K, and **c**, **f** for T_{in} = 633 K, respectively. The parity diagrams and the measured profiles over their full length of 30 mm are depicted in the supporting information (Sections S10-11).

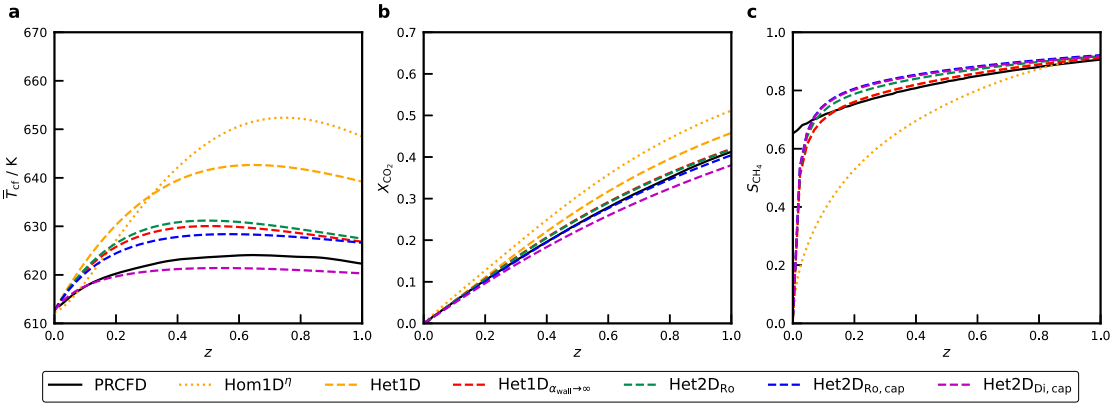

Fig. 4. Comparison of results obtained using PRCFD and one- and two-dimensional pseudo-continuum models for an inlet temperature T_{in} = 613 K. **a** Temperature, **b** carbon dioxide conversion, and **c** selectivity to methane. The employed boundary conditions at the bed inlet for the PRCFD lead to a high initial selectivity, which cannot be reproduced by the continuum models.

boundary conditions, but starts at significantly lower values in the pseudo-continuum models. This discrepancy can be clearly attributed to the consecutive reactions of rWGS and CO methanation, coupled with the axial discretization, which does not allow for significant reaction rates of the CO methanation reaction at low values of z. However, as indicated by the comparison of the one-dimensional homogeneous and heterogeneous continuum models Hom1D$^{\eta}$ and Het1D, respectively, a heterogeneous approach significantly improves the prediction of the selectivity, as well as the temperature and conversion. Since heterogeneous continuum models consider intraparticle concentration gradients, the consecutive reaction network of rWGS and CO methanation reactions can be better represented. This finding emphasizes that the catalyst effectiveness factor derived from the Thiele modulus used in homogeneous continuum models is not applicable to reaction networks (Handbook of heterogeneous catalysis, 1997). Therefore, the following discussion will only concern heterogeneous continuum models.

In the one-dimensional model Het1D, the overall heat transfer is significantly underestimated, causing a temperature excess of about 20 K compared to the PRCFD and, accordingly, an increased conversion. Similar observations, especially at low Reynolds numbers, have been reported by Dixon (2021) in the context of the partial oxidation of ethylene. With the two-dimensional continuum model Het2D$_{Ro}$, the temperature overshoot in the hot spot decreases to approximately 10 K, with a corresponding end-of-pipe conversion only slightly higher than that

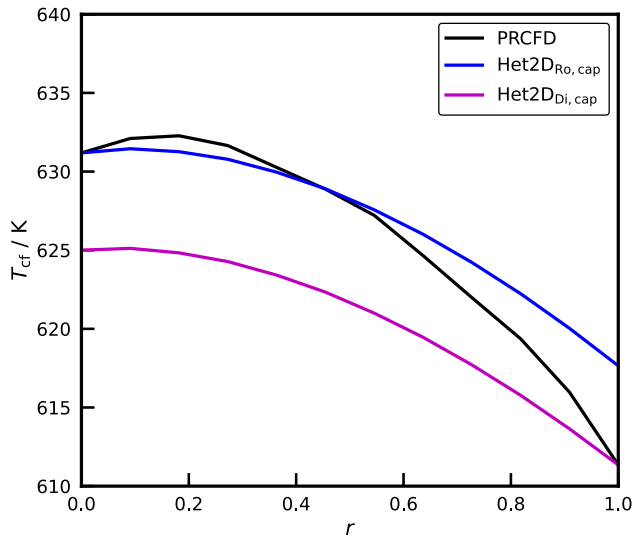

Fig. 5. Radial profiles of T_{cf} at the hot spot ($T_{in} = 613\,K$, $z = 0.6$) from the PRCFD in comparison to those from Het2D$_{Ro,cap}$ and Het2D$_{Di,cap}$.

predicted by the PRCFD simulations. In two-dimensional models, the radial heat transfer is calculated based on the effective radial thermal conductivity, eliminating the need to apply a separate correlation for the overall radial heat transfer. Apart from the first increments, the selectivity to methane is slightly overestimated by the continuum model but steadily converges to the results from the PRCFD toward the end-of-pipe. This general behavior can be observed for all two-dimensional models. A stainless steel capillary runs along the center of the reactor and, due to its high thermal conductivity, affects both the radial temperature profile through heat transfer from the fluid phase to the capillary and the axial temperature profile through thermal conduction along the capillary. Results from the PRCFD simulations suggest that the amount of thermal energy released through the capillary from the fixed bed corresponds to approximately 9 % of the total generated heat and should therefore be taken into account (SI Section S5). Compared to model Het2D$_{Ro}$, model Het2D$_{Ro,cap}$ behaves as expected, yielding a hot spot temperature reduced by approximately 3 to 4 K and a generally slightly broadened temperature profile. Nonetheless, model Het2D$_{Ro,cap}$ still overestimates the hot spot temperature by about 6 K.

The applied α_{wall}-model introduces an artificial temperature jump at the tube and capillary walls to account for the increased heat transport resistance at the walls. It is well known that the temperature jump resulting from the α_{wall}-model leads to an inaccurate description of temperatures close to the walls, particularly for fixed beds with small tube-to-particle ratios (see Figures 5 and 6c,d) (Dixon, 2012). To test the impact of the α_{wall} on the temperature distribution in the fixed bed, the heat transfer between packed bed and wall is neglected by setting $\alpha_{wall} \to \infty$ in the one-dimensional model Het1D$_{\alpha_{wall}\to\infty}$, and by implementing Dirichlet boundary conditions at the interfaces between the continuous phase and the reactor wall, as well as the capillary, in two-dimensional models (Het2D$_{Di,cap}$).

Figure 5 shows the radial temperature profiles obtained from the PRCFD and the heterogeneous continuum models Het2D$_{Ro,cap}$ and Het2D$_{Di,cap}$ at $z = 0.6$. The radial profile from the PRCFD generally lies between those of the two continuum models, while the ordinary model Het2D$_{Ro,cap}$ better describes the temperature toward the reactor core. Increasing α_{wall}, resulting in model Het2D$_{Di,cap}$, leads to improved accuracy toward the reactor wall. This observation is also visible in the axial profiles, where model Het2D$_{Di,cap}$ yields significantly lower temperatures and conversion compared to Het2D$_{Ro,cap}$. Accordingly, model Het1D$_{\alpha_{wall}\to\infty}$ leads to about 15 K lower temperatures than model Het1D, achieving the best agreement with the PRCFD simulations of all the one-dimensional models investigated. Nevertheless, the discrepancy between model Het1D$_{\alpha_{wall}\to\infty}$ and the PRCFD is significant. This can be attributed to the fact that, in the studied cases, the assumption of a parabolic radial temperature profile when deriving the overall heat transfer coefficient is insufficient (Froment, 1962).

Figure 6 presents the two-dimensional temperature fields obtained from the PRCFD and the continuum models Het2D$_{Ro,cap}$ and Het2D$_{Di,cap}$, along with the standard deviation of the PRCFD results and the differences between the PRCFD and the two continuum models. The fields extracted from PRCFD are calculated by determining the arithmetic mean and standard deviation based on point seeds that are distributed equally (distance between seeds: 0.2 $d_{p,50}$) on circles with defined radii and axial positions. The temperature field obtained from the PRCFD (Figure 6a) emphasizes the shallow radial temperature profiles, while the narrow standard deviation (Figure 6b), caused by local inhomogeneities in the fixed bed, remains below 2 K. These local inhomogeneities can be exemplified by, for instance, non-rotational symmetric fixed bed structure, or by stagnant zones resulting from local fluid-dynamic effects. Intraparticle temperature distributions are evaluated in the supporting information (Section S12). As discussed, the continuum model Het2D$_{Ro,cap}$ overestimates the temperature while providing the best agreement with the PRCFD at the reactor core (Figure 6c,d), whereas model Het2D$_{Di,cap}$ (Figure 6e,f) predicts overall lower temperatures, with better agreement at the reactor wall. Overall, the discussion illustrates that continuum models with an increasing level of detail can describe the profile reactor increasingly well. However, with the employed assumptions and available correlations, significant sensitivities to intraparticle mass transport and interparticle heat transport are revealed, which have the potential to interfere with the quantitative evaluation of such profiles in the context of kinetic modeling and must therefore be adequately considered.

3.3. *Intraparticle mass transport phenomena - Concentration fields and catalyst effectiveness factor*

Next to interparticle temperature and concentration fields, heterogeneous models such as the PRCFD and Het2D$_{Di,cap}$ also allow one to resolve intraparticle profiles. Figure 7a shows the molar fraction field of carbon monoxide in an axial plane through the reactor, with magnifications of single particles near the inlet and outlet of the reactor. These intraparticle concentration fields are emphasized in Figure 7b. The non-symmetric concentration profiles inside a catalyst particle, most prominently visible near the inlet of the reactor (Figure 7a), are the result of fluid-dynamic effects.

For catalyst particles near the inlet, the carbon monoxide concentration increases toward the particle interior, forming a maximum at approximately $r_c = 0.8$, whereas this maximum gradually disappears at higher axial coordinates until particles in the downstream section of the reactor show a monotonic decrease in the carbon monoxide concentration from the particle surface to the center. This profile is the result of an interplay between intraparticle mass transport and changes in the gas composition throughout the reactor. As shown in Figure 7b, this general trend is also well described with the continuum model Het2D$_{Di,cap}$. By applying the original formulation of the catalyst effectiveness factor,

$$\eta_j = \frac{\frac{1}{V_c}\int_V \dot{r}_j \,\mathrm{d}V}{\frac{1}{A_c}\int_A \dot{r}_j \,\mathrm{d}A}, \tag{4}$$

which relates the volume-averaged reaction rate inside the particle to the surface reaction rate, effectiveness factors of approximately $\eta_{COmeth} \approx 2$ and $\eta_{rWGS} \approx 0.5$ are obtained at the inlet of the fixed bed from both the PRCFD and the pseudo-continuum model (Figure 7c). Toward the outlet, the effectiveness factors converge to about 0.6 for both reactions. Such values of the effectiveness factor cannot be predicted by formulations based on the Thiele modulus, which are typically employed in homogeneous continuum models. The applied definition of the effec-

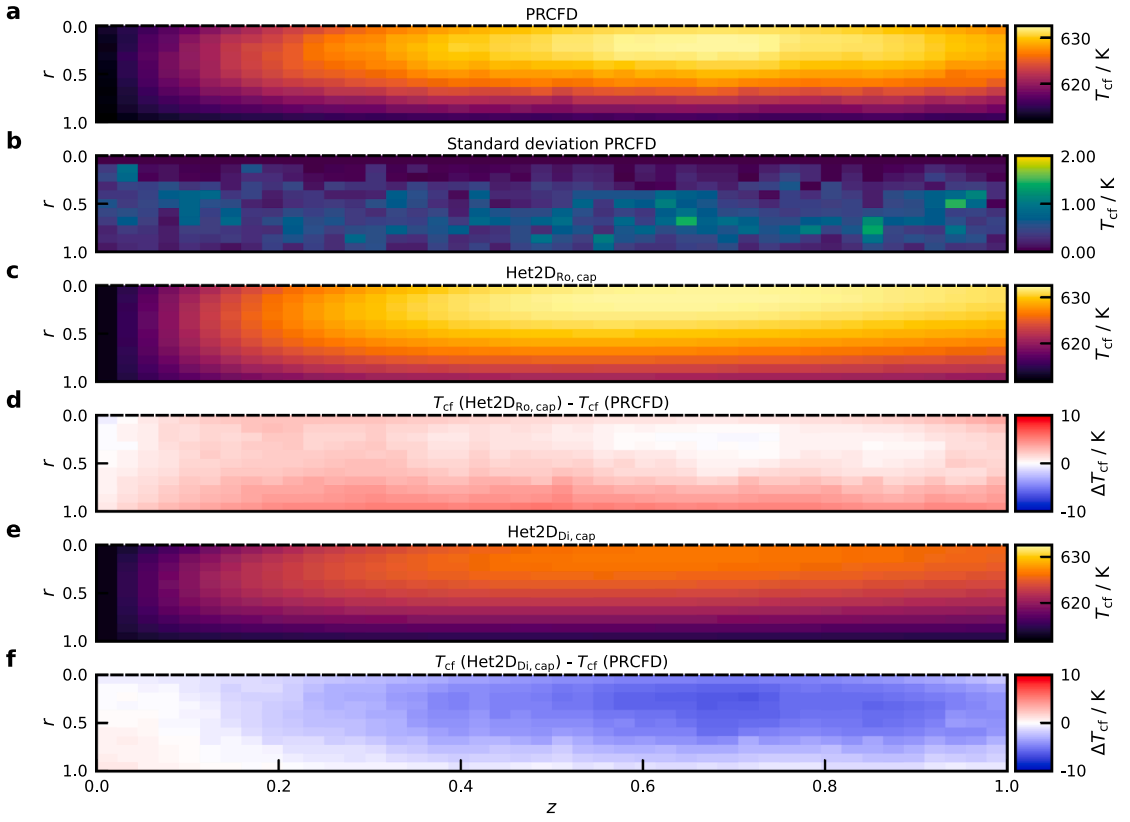

Fig. 6. 2D temperature fields for an inlet temperature $T_{in} = 613\,K$. **a** PRCFD, **b** standard deviation obtained from the PRCFD simulation, **c** model Het2D$_{Ro,cap}$, **d** temperature difference between Het2D$_{Ro,cap}$ and the PRCFD, **e** model Het2D$_{Di,cap}$, and **f** temperature difference between Het2D$_{Di,cap}$ and the PRCFD.

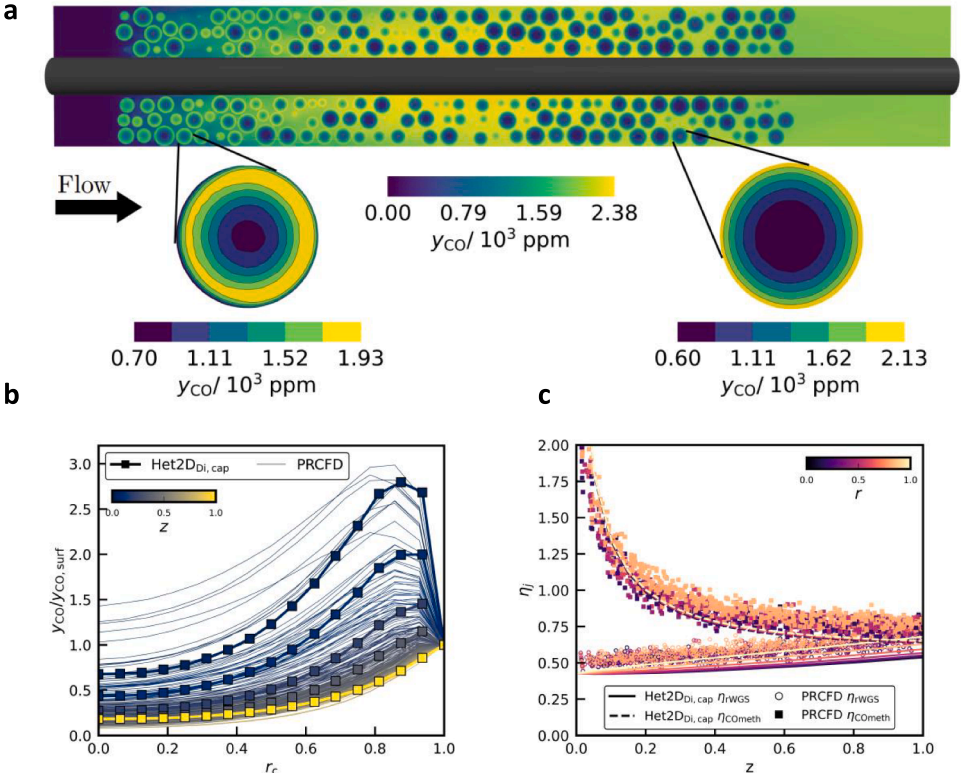

Fig. 7. **a** Molar fraction of carbon monoxide along a plane through the fixed bed center. **b** Circumferentially averaged radial profiles of the intraparticle carbon monoxide mole fraction, normalized by its value at the catalyst surface. **c** Comparison of the catalyst efficiency derived from pseudo-continuum model Het2D$_{Di,cap}$ and the PRCFD simulation. In **b** and **c**, results from the continuum model are depicted as lines, while the effectiveness factor is evaluated for every particle separately from the PRCFD results ($T_{in} = 613\,K$).

Table 4
Summary of f_k and coefficients of determination for the different models.

Model	f_k	$R^2_{T_{cf}}$	$R^2_{X_{CO_2}}$	$R^2_{S_{CH_4}}$
Hom1D$^{\eta}$	0.33	0.963	0.981	0.896
Het1D	0.41	0.993	0.952	0.994
Het1D$_{\alpha_{wall}\to\infty}$	0.62	0.999	0.980	0.999
Het2D$_{Ro}$	0.59	0.998	0.977	0.999
Het2D$_{Ro,cap}$	0.67	0.999	0.983	0.999
Het2D$_{Di,cap}$	1.13	0.996	0.999	0.994
Het1D w/o EB	0.93	n.a.	0.995	0.998

tiveness factor via the Thiele modulus is derived for a single first-order reaction within an isothermal pellet (Aris, 1957), hence $0 \leq \eta_j \leq 1$. This underscores why the considered reaction network cannot be adequately modeled using pseudo-homogeneous continuum models (Figure 4). Considering these observations collectively highlights why the utilization of heterogeneous pseudo-continuum models is crucial in systems posing selectivity problems under conditions that enable intraparticle mass-transport limitations.

3.4. Implications on the quantitative model-based evaluation of data obtained from profile reactors

As elucidated in Section 3.2, a higher degree of detail in the continuum models leads to an improved agreement with the results obtained from the PRCFD simulations under the investigated conditions. This implication must be considered when spatially resolved data from profile reactors are employed for quantitative, model-based evaluation, such as kinetic modeling, because continuum models of varying complexity can yield diverging kinetic parameters in the resulting parameter-estimation problem. To emphasize this crucial relationship, the kinetic rate constants $k_{COmeth/rWGS}$ are extended by a constant factor f_k, which is subsequently fitted to the results from the PRCFD simulations using the different continuum models (Table 3). In one specific case, the energy balance is removed from the calculation, and the experimentally measured temperature is introduced directly into the model (Het1D w/o EB).

The resulting values of f_k with each continuum model are summarized in Table 4, together with the corresponding coefficients of determination R^2 for T_{cf}, X_{CO_2}, and S_{CH_4}. These are not discussed in further detail here, but they confirm the trend observed in Figure 4, as expected: a higher deviation between model and PRCFD requires more significant correction factors f_k. For example, the kinetics with model Hom1D$^{\eta}$ must be scaled down by $f_k = 0.33$, and the selectivity is poorly predicted, while model Het2D$_{Di,cap}$ requires a much smaller correction and more accurately predicts temperature, conversion, and selectivity. This highlights how input and physical model uncertainties can superimpose the fitted intrinsic kinetic parameters when an inappropriate model is used for parameter estimation. Notably, the overall best fit is reached with model Het1D w/o EB, which does not evaluate the energy balance. In this case, the measured mean axial fluid temperature is directly inserted into the model to derive the reaction rates. Several authors have employed this approach for estimating kinetic parameters based on spatially resolved experiments (Hernandez Lalinde et al., 2020; Cholewa et al., 2024; Küchen et al., 2024). In this context, this is a generous simplification, since the inaccurate modeling of heat transfer does not negatively affect the estimated parameters, and the simple one-dimensional models ensure a low computational effort. The conditions that must be met for this simplification to be made are discussed in the following section.

The fundamental assumption of the applied sampling technique, which uses a capillary to extract a gaseous sample in the profile reactor, is that the measured temperature and gas composition represent a radial average. Rate equations, such as the kinetics implemented in this work, usually do not depend linearly on their variables. For example, temperatures influence the rates exponentially, and partial pressures contribute with exponents between 0.5 and 3. Accordingly, the use of average values can lead to incorrect conclusions if the non-linearities are not properly accounted for. In this context, the conducted PRCFD calculations revealed a very narrow standard deviation of the radially and circumferentially averaged profiles of the species' molar fractions (see Figure 3), indicating a radially homogeneous gas-phase composition. Therefore, no uncertainties arising from the non-linear contributions of partial pressures are to be expected. This is not the case for the temperature. In the hot spot region (see Figure 3e), the temperature difference ΔT_{cf} between the wall temperature T_{wall} and the average temperature $\bar{T}_{cf}$ reaches around 15 K which cannot be simply assumed as radially isothermal. To check whether calculating the reaction rates based on the measured mean temperature differs from radially averaging the actual rates itself, the reaction rates and temperature fields from the model Het2D$_{Di,cap}$ are used. Figure 8a shows the axially resolved ratios of the radially averaged reaction rates $\bar{r}_j$ to $r_j(\bar{T}_{cf})$, the reaction rate calculated based on the average temperature $\bar{T}_{cf}$. At $z = 0$, both reaction rates are similar due to the applied boundary conditions. For the rWGS reaction, the maximum deviation between the two rates occurs around the temperature hot spot and reaches approximately 1 %. The CO methanation reaction reveals less pronounced differences in the rate. These low deviations between the two ways to calculate the reaction rates indicate that, within the occurring temperature window, the rate equations can be linearized with satisfying accuracy.

This assumption is further discussed in Figure 8b, where the temperature-dependent reaction rates are depicted in both their original and linearized forms. The rates are linearized using a first-order Taylor expansion around $\bar{T}_{cf}$ at the hot spot:

$$r_{j,\mathrm{lin},\bar{T}_{cf}}(T_{cf}) = r_j(\bar{T}_{cf}) + \left.\frac{dr_j}{dT_{cf}}\right|_{\bar{T}_{cf}} (T_{cf} - \bar{T}_{cf}) \tag{5}$$

Within the considered temperature range, which is assumed to span symmetrically by $\Delta T_{cf} = \bar{T}_{cf} - T_{wall}$ around $\bar{T}_{cf}$, the average deviation is 1.45 % and the maximum deviation is 4.61 % for the rWGS reaction, clearly showing that the respective rate equation can be linearized around $\bar{T}_{cf}$ with sufficient accuracy. The rate equation for the CO methanation reaction can be linearized even more accurately. In combination with the shallow radial temperature profiles (Figure 6a and e) and the low radial standard deviation of the gas-phase composition, this characteristic convincingly explains why $r_j(\bar{T}_{cf})$ satisfactorily represents the reaction inside the profile reactor, which is ultimately assumed when model Het1D w/o EB is used to derive kinetic parameters. It should also be noted that the considered temperature window is chosen rather conservatively with respect to the upper boundary, since the maximum temperature simulated at the hot spot location, $T_{cf,max} = 633.4$ K, is well within the temperature window.

In general, the reaction rates must be adequately linearizable within the considered temperature range to apply the measured mean temperatures in the estimation of the kinetic parameters. This depends on the kinetic rate equations and the temperature range across the cross section. Since the rate equations are a-priori unknown, the linearizability of the reaction rates can only be checked after parameter estimation by assuming the maximum temperature of the cross section. The error in the reaction rates caused by using the mean average temperature is always smaller than the maximum error of the rate equation linearization. However, the actual size of the error can only be quantified by knowing the radial temperature profile. Nevertheless, neglecting the energy balance in a computationally efficient one-dimensional model is reasonable, if the maximum error of the rate equation linearization is smaller 5 %. Therefore, the following criterion can be defined based on the maximal relative deviation between the reaction rate linearized around the measured hot spot temperature and the original reaction rate:

$$\max_{T\in[\bar{T}_{f,max}-\Delta T,\bar{T}_{f,max}+\Delta T]} \left(\left| \frac{r_{j,\mathrm{lin},\bar{T}_{f,max}}(T) - r_j(T)}{r_j(T)} \right| \right) \leq 0.05 \tag{6}$$

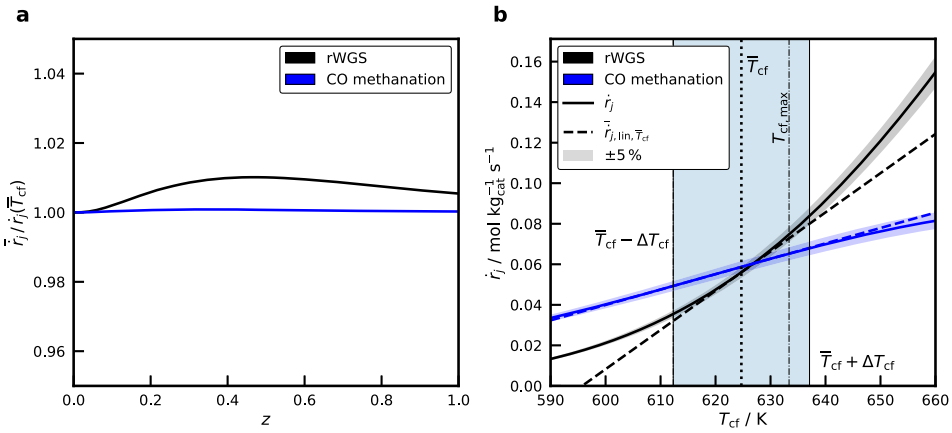

Fig. 8. **a** Ratio between the radially averaged reaction rates $\bar{r}_j$ and $\dot{r}_j(\bar{T}_{cf})$, the reaction rate calculated using the radially averaged temperature $\bar{T}_{cf}$, for the rWGS and CO methanation reactions along the reactor as calculated with model Het2D$_{Di,cap}$. **b** Temperature-dependent reaction rates $\dot{r}_j$ of the rWGS and CO methanation reactions, shown both in their original form and linearized using a first-order Taylor approximation around $\bar{T}_{cf}$ at the temperature hot spot. The shaded temperature regime provides a conservative estimate of the occurring temperatures inside the reactor ($T_{in} = 613$ K).

with $\Delta T = \bar{T}_{f,max} - T_{wall}$, where $\bar{T}_{f,max}$ is the measured hot spot temperature. This criterion needs to be fulfilled for all reactions j in the investigated reaction network. Under these conditions, directly incorporating the experimentally measured temperature into the continuum model as a replacement for evaluating the energy balance does not negatively affect the derivation of kinetic parameters. In fact, this procedure also eliminates uncertainties regarding the accurate description of heat transfer inside profile reactors, ultimately increasing the accuracy of kinetic parameters derived from data obtained in profile reactors. It should be noted that the operating conditions and the properties of the fixed bed used in this study were selected to ensure well-defined characteristics that can be accurately calculated using PRCFD, thereby allowing conclusions to be drawn on appropriate modeling strategies. In the context of reaction kinetics, the influence of intraparticle mass transport limitations should be significantly reduced, for example through more highly diluted feeds and smaller catalyst particles.

4. Conclusion

Detailed particle-resolved CFD simulations of a laboratory-scale profile reactor were conducted and validated against experimental data for the CO_2 methanation reaction. Insights into the local temperature, concentration, and velocity fields derived from the PRCFD were used to evaluate the applicability of pseudo-continuum models of different levels of detail in the context of fitting kinetic parameters, which first and foremost requires a clear distinction between intrinsic kinetic processes and superimposed transport effects. At a glance, homogeneous pseudo-continuum models proved incapable of resolving selectivity problems under pore-diffusion-limited conditions. Employing heterogeneous pseudo-continuum models yields better selectivities, but even when considering the influence of the thermally conductive sampling capillary on the temperature field in the reactor and adjusted boundary conditions, significant model uncertainties remained, which ultimately can alter the derived kinetic parameters. To avoid these uncertainties, the measured temperatures from the profile reactor can, in principle, be directly introduced into a comparatively simple one-dimensional model, thereby replacing the evaluation of the energy balance for fitting kinetic parameters. By avoiding the described model uncertainties, this approach can provide improved results. However, since distinct radial temperature profiles can occur in profile reactors, this approach requires kinetic rate equations that can be sufficiently linearized with respect to temperature. Based on results from the PRCFD and continuum models, we suggest a criterion that should be evaluated after the parameter fit in order for this simplification to be valid. This criterion incorporates the wall temperature and the measured average gas-phase temperature, both of which are directly available from profile reactor measurements, as well as the kinetic rate equations, and can therefore be easily verified numerically.

Ideally, to allow for precise results, experiments in the profile reactor for kinetic studies should from the outset be conducted under conditions that limit the influence of intraparticle transport limitations and radial temperature gradients. As a starting point, this can be facilitated through catalyst particle sizes well below 500 µm, depending on the chosen support material, dilution of the fixed bed, and generally a diluted feed composition such as 75 % inert. Future PRCFD investigations of profile reactors should focus on fluid-dynamic effects inside the reactor. In particular, it is still not fully understood which fraction of the overall gas-phase flow passes through the orifices in the capillary and whether this flow represents a true average of the gas-phase composition and temperature. Further PRCFD simulations coupled with an advanced optimization algorithm, such as Bayesian optimization, can be used to determine the optimal conditions for kinetic measurements (Hu et al., 2026). Overall, this study enhances the understanding of the conditions inside profile reactors and improves their application in reaction engineering research, where such reactors are increasingly used as efficient tools for acquiring data for kinetic studies.

CRediT authorship contribution statement

Gerrit Küchen: Writing – review & editing, Writing – original draft, Visualization, Validation, Methodology, Investigation, Formal analysis, Conceptualization; **Martin Kutscherauer:** Writing – review & editing, Writing – original draft, Validation, Methodology, Investigation, Formal analysis, Conceptualization; **Stefan Rudolph:** Investigation; **Gregor D. Wehinger:** Writing – review & editing, Supervision, Resources; **Thomas Turek:** Writing – review & editing, Supervision, Resources.

Data availability

Research data associated with this article is publicly available at 10.5281/zenodo.18872576.

Declaration of competing interest

The authors declare that they have no known competing financial interests or personal relationships that could have appeared to influence the work reported in this paper.

Funding

This research did not receive any specific grant from funding agencies in the public, commercial, or not-for-profit sectors.

Acknowledgments

The authors acknowledge support by the state of Baden-Württemberg through bwHPC.

Supplementary material

Supplementary material associated with this article can be found in the online version at 10.1016/j.ces.2026.124245.

References

Handbook of heterogeneous catalysis, 1997. Handbook of heterogeneous catalysis. In: Ertl, G., Knözinger, H., Weitkamp, J. (Eds.), Handbook of Heterogeneous Catalysis. Wiley-VCH, Weinheim, pp. 1235–1242.

Aris, R., 1957. On shape factors for irregular particles—I: The steady state problem. Diffusion and reaction. Chemical Engineering Science 6 (6), 262–268. https://doi.org/10.1016/0009-2509(57)85028-3

Berg, V., Geske, M., Korup, O., Schmidt, M., Rosowski, F., Karpov, A., Kraemer, M., Horn, R., 2024. Selective Oxidation of Ethylene to Ethylene Oxide on Silver Catalysts at Industrial Conditions: Reactor Profiles, Kinetics, and Chlorine Inhibition. Industrial & Engineering Chemistry Research 63 (9), 3891–3909. https://doi.org/10.1021/acs.iecr.3c04345

Burger, T., Donaubauer, P., Hinrichsen, O., et al., 2021. On the kinetics of the co-methanation of CO and CO_2 on a co-precipitated Ni-Al catalyst. Applied Catalysis B: Environmental 282, 119408. https://doi.org/10.1016/j.apcatb.2020.119408

Cholewa, T., Steinbach, B., Heim, C., Nestler, F., Nanba, T., Güttel, R., Salem, O., 2024. Reaction kinetics for ammonia synthesis using ruthenium and iron based catalysts under low temperature and pressure conditions. Sustainable Energy & Fuels 8 (10), 2245–2255. https://doi.org/10.1039/D4SE00254G

Dixon, A.G., 2012. Fixed bed catalytic reactor modelling—the radial heat transfer problem. The Canadian Journal of Chemical Engineering 90 (3), 507–527. https://doi.org/10.1002/cjce.21630

Dixon, A.G., 2021. Local transport and reaction rates in a fixed bed reactor tube: Exothermic partial oxidation of ethylene. Chemical Engineering Science 231, 116305. https://doi.org/10.1016/j.ces.2020.116305

Dixon, A.G., Nijemeisland, M., Stitt, E.H., 2013-01. Systematic mesh development for 3d CFD simulation of fixed beds: Contact points study. Computers & Chemical Engineering 48, 135–153. https://doi.org/10.1016/j.compchemeng.2012.08.011

Dixon, A.G., Partopour, B., 2020. Computational fluid dynamics for fixed bed reactor design. Annual Review of Chemical and Biomolecular Engineering 11, 109–130. https://doi.org/10.1146/annurev-chembioeng-092319-075328

Donaubauer, P.J., Hinrichsen, O., 2019. Evaluation of Effectiveness Factors for Multicomponent Diffusion Models Inside 3D Catalyst Shapes. Industrial & Engineering Chemistry Research 58 (1), 110–119. https://doi.org/10.1021/acs.iecr.8b04922

Elnashaie, S.S.E.H., Abashar, M.E.E., 1993. Steam reforming and methanation effectiveness factors using the dusty gas model under industrial conditions. Chemical Engineering and Processing: Process Intensification 32 (3), 177–189. https://doi.org/10.1016/0255-2701(93)80014-8

Eppinger, T., Seidler, K., Kraume, M., 2011. DEM-CFD simulations of fixed bed reactors with small tube to particle diameter ratios. Chemical Engineering Journal 166 (1), 324–331. https://doi.org/10.1016/j.cej.2010.10.053

Fischer, K.L., Langer, M.R., Freund, H., 2019. Dynamic carbon dioxide methanation in a wall-cooled fixed bed reactor: Comparative evaluation of reactor models. Industrial & Engineering Chemistry Research 58 (42), 19406–19420. https://doi.org/10.1021/acs.iecr.9b02863

Friedland, J., Kreitz, B., Grimm, H., Turek, T., Güttel, R., 2020. Measuring Adsorption Capacity of Supported Catalysts with a Novel Quasi–Continuous Pulse Chemisorption Method. ChemCatChem 12 (17), 4373–4386. https://doi.org/10.1002/cctc.202000278

Froment, G.F., 1962. Design of fixed-bed catalytic reactors based on effective transport models. Chemical Engineering Science 17 (11), 849–859. https://doi.org/10.1016/0009-2509(62)87017-1

Hernandez Lalinde, J.A., Kofler, K., Huang, X., Kopyscinski, J., et al., 2018. Improved Kinetic Data Acquisition Using An Optically Accessible Catalytic Plate Reactor with Spatially-Resolved Measurement Techniques. Case of Study: CO_2 Methanation. Catalysts 8 (2), 86. https://doi.org/10.3390/catal8020086

Hernandez Lalinde, J.A., Roongruangsree, P., Ilsemann, J., Bäumer, M., Kopyscinski, J., et al., 2020. CO_2 methanation and reverse water gas shift reaction. Kinetic study based on in situ spatially-resolved measurements. Chemical Engineering Journal 390, 124629. https://doi.org/10.1016/j.cej.2020.124629

Horn, R., Degenstein, N.J., Williams, K.A., Schmidt, L.D., 2006. Spatial and temporal profiles in millisecond partial oxidation processes. Catalysis Letters 110 (3-4), 169–178. https://doi.org/10.1007/s10562-006-0117-8

Horn, R., Korup, O., Geske, M., Zavyalova, U., Oprea, I., Schlögl, R., et al., 2010. Reactor for *in situ* measurements of spatially resolved kinetic data in heterogeneous catalysis. Review of Scientific Instruments 81 (6), 064102. https://doi.org/10.1063/1.3428727

Horn, R., Williams, K.A., Degenstein, N.J., Schmidt, L.D., et al., 2007. Mechanism of H_2 and CO formation in the catalytic partial oxidation of CH_4 on Rh probed by steady-state spatial profiles and spatially resolved transients. Chemical Engineering Science 62 (5), 1298–1307. https://doi.org/10.1016/j.ces.2006.11.030

Hu, T., Qin, L., Zhou, L., Zheng, X., Zhu, L.-T., 2026. Analysis and optimization of methanol production and temperature gradient in CO_2 hydrogenation fixed bed reactors using CFD and Bayesian optimization. Chemical Engineering Science 321, 123030. https://doi.org/10.1016/j.ces.2025.123030

Jurtz, N., Kraume, M., Wehinger, G.D., 2019. Advances in fixed-bed reactor modeling using particle-resolved computational fluid dynamics (CFD). Reviews in Chemical Engineering 35 (2), 139–190. https://doi.org/10.1515/revce-2017-0059

Kopyscinski, J., Schildhauer, T.J., Vogel, F., Biollaz, S. M.A., Wokaun, A., et al., 2010. Applying spatially resolved concentration and temperature measurements in a catalytic plate reactor for the kinetic study of CO methanation. Journal of Catalysis 271 (2), 262–279. https://doi.org/10.1016/j.jcat.2010.02.008

Korup, O., Mavlyankariev, S., Geske, M., Goldsmith, C.F., Horn, R., et al., 2011. Measurement and analysis of spatial reactor profiles in high temperature catalysis research. Chemical Engineering and Processing: Process Intensification 50 (10), 998–1009. https://doi.org/10.1016/j.cep.2011.05.024

Koschany, F., Schlereth, D., Hinrichsen, O., et al., 2016. On the kinetics of the methanation of carbon dioxide on coprecipitated $NiAl(O)_x$. Applied Catalysis B: Environmental 181, 504–516. https://doi.org/10.1016/j.apcatb.2015.07.026

Kreitz, B., Wehinger, G.D., Turek, T., 2019. Dynamic simulation of the CO_2 methanation in a micro-structured fixed-bed reactor. Chemical Engineering Science 195, 541–552. https://doi.org/10.1016/j.ces.2018.09.053

Kutscherauer, M., 2024. Particle-resolved CFD simulation of catalytic fixed bed reactors for maleic anhydride production. Ph.D. thesis. Clausthal University of Technology. https://doi.org/10.21268/20240522-0

Kutscherauer, M., Anderson, S.D., Böcklein, S., Mestl, G., Turek, T., Wehinger, G.D., 2024. A conjugated heat and mass transfer model to implement reaction in particle-resolved CFD simulations of catalytic fixed bed reactors. Engineering Applications of Computational Fluid Mechanics 18 (1), 2292100. https://doi.org/10.1080/19942060.2023.2292100

Kutscherauer, M., Böcklein, S., Mestl, G., Turek, T., Wehinger, G.D., 2022. An improved contact modification routine for a computationally efficient CFD simulation of packed beds. Chemical Engineering Journal Advances 9, 100197. https://doi.org/10.1016/j.ceja.2021.100197

Kutscherauer, M., Reinold, P., Böcklein, S., Mestl, G., Turek, T., Wehinger, G.D., 2023. How Temperature Measurement Impacts Pressure Drop and Heat Transport in Slender Fixed Beds of Raschig Rings. ACS Eng. Au 3 (1), 45–58. https://doi.org/10.1021/acsengineeringau.2c00039

Kutscherauer, M., Wehinger, G.D., 2025. Particle-resolved CFD simulation of diluted catalytic fixed bed reactors for formaldehyde production. ACS Engineering Au 5 (3), 284–297. https://doi.org/10.1021/acsengineeringau.5c00012

Küchen, G., Gottheil, L., Olszok, V., Weber, A.P., Bremer, J., Turek, T., 2026. Detailed Spatially Resolved Gas-Phase Investigations of CO_2 Methanation on a Ni/SiO_2 Catalyst: Insights into the Reaction Pathway and Efficient Kinetic Parameter Estimation. Industrial & Engineering Chemistry Research . https://doi.org/10.1021/acs.iecr.5c04764

Küchen, G., Olszok, V., Kreitz, B., Mahr, C., Rosenauer, A., Turek, T., Weber, A.P., Wehinger, G.D., 2024. Spray-dried Ni-Co bimetallic catalysts for dry reforming of methane. ChemCatChem 16 (17), e202400371. https://doi.org/10.1002/cctc.202400371

Küchen, G., Turek, T., 2026. Measuring spatiotemporal concentration and temperature profiles in a tubular fixed-bed reactor for CO_2 methanation. ChemCatChem 18 (1), e01636. https://doi.org/10.1002/cctc.202501636

Langer, M., Freund, H., 2024. Reaction Kinetic Modeling of the CO_x Methanation over a Broad Range of Operation Conditions on an Impregnated Ni/Al_2O_3 Catalyst. Industrial & Engineering Chemistry Research 63 (25), 10981–10996. https://doi.org/10.1021/acs.iecr.4c00819

Langer, M., Kellermann, D., Freund, H., et al., 2023. Kinetic modeling of dynamically operated heterogeneously catalyzed reactions: Microkinetic model reduction and semi-mechanistic approach on the example of the CO_2 methanation. Chemical Engineering Journal 467, 143217. https://doi.org/10.1016/j.cej.2023.143217

Lee, W.J., Li, C., Prajitno, H., Yoo, J., Patel, J., Yang, Y., Lim, S., et al., 2021. Recent trend in thermal catalytic low temperature CO_2 methanation: A critical review. Catalysis Today 368, 2–19. https://doi.org/10.1016/j.cattod.2020.02.017

Maffei, T., Gentile, G., Rebughini, S., Bracconi, M., Manelli, F., Lipp, S., Cuoci, A., Maestri, M., 2016. A multiregion operator-splitting CFD approach for coupling microkinetic modeling with internal porous transport in heterogeneous catalytic reactors. Chemical Engineering Journal 283, 1392–1404. https://doi.org/10.1016/j.cej.2015.08.080

Partopour, B., Dixon, A.G., 2017. An integrated workflow for resolved-particle packed bed models with complex particle shapes. Powder Technology 322, 258–272. https://doi.org/10.1016/j.powtec.2017.09.009

Partopour, B., Dixon, A.G., 2018. n-butane partial oxidation in a fixed bed: A resolved particle computational fluid dynamics simulation. The Canadian Journal of Chemical Engineering 96 (9), 1946–1956. https://doi.org/10.1002/cjce.23130

Pichler, M., Haddadi, B., Jordan, C., Norouzi, H., Harasek, M., 2021-01. Effect of particle contact point treatment on the CFD simulation of the heat transfer in packed beds. Chemical Engineering Research and Design 165, 242–253. https://doi.org/10.1016/j.cherd.2020.11.005

Rönsch, S., Schneider, J., Matthischke, S., Schlüter, M., Götz, M., Lefebvre, J., Prabhakaran, P., Siegfried, B., et al., 2016. Review on methanation – From fundamentals to current projects. Fuel 166, 276–296. https://doi.org/10.1016/j.fuel.2015.10.111

Schmider, D., Maier, L., Deutschmann, O., et al., 2021. Reaction Kinetics of CO and CO_2 Methanation over Nickel. Industrial & Engineering Chemistry Research 60 (16), 5792–5805. https://doi.org/10.1021/acs.iecr.1c00389

Shirsath, A.B., Schulte, M.L., Kreitz, B., Tischer, S., Grunwaldt, J.-D., Deutschmann, O., et al., 2023. Spatially-resolved investigation of CO_2 methanation over Ni/γ-Al_2O_3 and $Ni_{3.2}Fe$/γ-Al_2O_3 catalysts in a packed-bed reactor. Chemical Engineering Journal 469, 143847. https://doi.org/10.1016/j.cej.2023.143847

Siemens Digital Industries Software, 2023. Simcenter STAR-CCM+ 23.10. https://www.plm.automation.siemens.com/global/de/products/simcenter/STAR-CCM.html.

Wehinger, G.D., Ambrosetti, M., Cheula, R., Ding, Z.-B., Isoz, M., Kreitz, B., Kuhlmann, K., Kutscherauer, M., Niyogi, K., Poissonnier, J., Réocreux, R., Rudolf, D., Wagner, J., Zimmermann, R., Bracconi, M., Freund, H., Krewer, U., Maestri, M., 2022. Quo vadis multiscale modeling in reaction engineering? – a perspective. Chemical Engineering Research and Design 184, 39–58. https://doi.org/10.1016/j.cherd.2022.05.030

Wehinger, G.D., Kraume, M., Berg, V., Korup, O., Mette, K., Schlögl, R., Behrens, M., Horn, R., 2016. Investigating dry reforming of methane with spatial reactor profiles and particle-resolved CFD simulations. AIChE J. 62 (12), 4436–4452. https://doi.org/10.1002/aic.15520

Wolke, F., Hu, Y., Schmidt, M., Korup, O., Horn, R., Reichelt, E., Jahn, M., Michaelis, A., et al., 2021. Spatially-resolved reaction profiles in Fischer-Tropsch synthesis – influence of operating conditions and promotion for iron-based catalysts. Catalysis Communications 158, 106335. https://doi.org/10.1016/j.catcom.2021.106335

Wollak, B., Doronkin, D.E., Espinoza, D., Sheppard, T., Korup, O., Schmidt, M., Alizadehfanaloo, S., Rosowski, F., Schroer, C., Grunwaldt, J.-D., Horn, R., 2022. Exploring catalyst dynamics in a fixed bed reactor by correlative operando spatially-resolved structure-activity profiling. Journal of Catalysis 408, 372–387. https://doi.org/10.1016/j.jcat.2021.08.029

Xu, J., Froment, G.F., 1989. Methane steam reforming, methanation and water-gas shift: I. Intrinsic kinetics. AIChE Journal 35 (1), 88–96. https://doi.org/10.1002/aic.690350109